A 2D/2D BiPO$_4$/g-C$_3$N$_4$-B Z-type heterojunction for enhanced photocatalytic degradation of dye pollutants

Hong-jian Zhao[*,†], **Yan Zhou**[*], **Ren-Jang Wu**[**], **Zheng-bing Han**[*], **Xu Li**[*], **and Zhe Yu**[*]

*College of Chemistry and Chemical Engineering, NingXia Normal University, Guyuan 756000, PRC
**Department of Applied Chemistry, ProvidenceUniversity, Taichung, Shalu, Taiwan, R.O.C

Abstract−A 2D/2D BiPO$_4$/g-C$_3$N$_4$-B nano-sheet heterojunction photocatalyst was synthesized via a simple coprecipitation method at room temperature using glacial acetic acid as solvent, which showed excellent activity toward the degradation of rhodamine B (RhB). The heterojunction showed much higher efficiency of separation and transfer of photogenerated carriers compared to that of its constituents. Moreover, the spectral response range of BiPO$_4$ was effectively broadened after the combination of g-C$_3$N$_4$-B and BiPO$_4$. Consequently, a 97.3% degradation of RhB within 25 min by BiPO$_4$/g-C$_3$N$_4$-B heterojunction photocatalyst under visible light irradiation was observed. The difference in work functions of BiPO$_4$ and g-C$_3$N$_4$-B was evident from UPS characterization, which led to the bending of the energy band and the establishment of an internal electric field at the interface of the heterojunction. Therefore, the synthesized direct Z-type BiPO$_4$/g-C$_3$N$_4$-B heterojunction enhanced the oxidation-reduction ability by promoting the effective separation of photogenerated carriers.

Keywords: 2D/2D Heterojunction, Z-type Heterojunction, BiPO$_4$, g-C$_3$N$_4$-B, Photocatalysis

INTRODUCTION

With rapid development, various dyes originating from the clothing, paper, and paint industries are continuously polluting the water resources on which humans rely for survival. These toxic dyes are difficult to degrade and adversely affect human health and safety. Modernized and developed water pollution treatment technologies have tried to solve these problems. For example, Bismuth-based materials, such as Bi$_2$O$_3$ [1], BiPO$_4$ [2], BiVO$_4$ [3], Bi$_2$WO$_6$ [4], and Bi$_2$O$_2$CO$_3$ [5], have been developed, which exhibit high photocatalytic activity toward water purification via degradation of harmful pollutants. They decompose pollutants into H$_2$O, CO$_2$, and other substances via photodegradation that are not harmful to the environment and unable to cause secondary pollution. This is an efficient, green, and sustainable solution to environmental pollution and a promising technical strategy. Among these materials, BiPO$_4$ exhibits high photocatalytic activity under ultraviolet light, with high photothermal stability, low cost, and non-toxic characteristics. Although it has great potential for further development [6], its wide band gap limits its utilization of solar energy [7]. Therefore, it is often combined with narrow band gap semiconductors to build a heterojunction with a reduced band gap, broadened spectral response range, enhanced photo-induced interfacial charge transfer, and suppressed recombination of photogenerated carriers. For example, heterojunctions, such as Bi-BiOBr/BiPO$_4$ [8], Fe$_3$O$_4$/BiPO$_4$ [9], CQDs/Ag$_3$PO$_4$/BiPO$_4$ [10], BiPO$_4$/Bi$_2$O$_2$CO$_3$ [11], and BiPO$_4$/Bi$_4$O$_5$I$_2$ [12], have been developed to improve the photocatalytic performance of BiPO$_4$ under visible light.

Recently, graphite-phase carbon nitride (g-C$_3$N$_4$) has emerged as a typical two-dimensional non-metallic polymer semiconductor photocatalyst material. It has many advantages, such as excellent optical, chemical, and thermal stability, various low-cost and facile synthetic methods, a rich source of elements, environment-friendly nature (as it is free of heavy metals), visible light response, good electronic acceptance and transport capacity. Simultaneously, g-C$_3$N$_4$ can easily be coated on the surface of other compounds, as it is a soft polymer material. It has already become a common candidate material in various application fields and is attracting more and more attention [13]. Of late, scientific research has been focused on the construction of heterojunction composite photocatalysts comprising BiPO$_4$ and g-C$_3$N$_4$ [14-16]. However, most of these BiPO$_4$/g-C$_3$N$_4$ materials are micro-sized block aggregate structures, which reduces the contact area of g-C$_3$N$_4$ and BiPO$_4$ and the number of active sites. The photocatalytic activity of these materials needs to be improved. On the other hand, boron (B) doped g-C$_3$N$_4$ can stably anchor the active N atoms exposed on the surface of g-C$_3$N$_4$ and can effectively inhibit the photo-carrier recombination of g-C$_3$N$_4$ [17]. Therefore, in this work, the B-doped g-C$_3$N$_4$ nano-sheet (g-C$_3$N$_4$-B) was combined with the BiPO$_4$ nano-round chips to form a 2D/2D BiPO$_4$/g-C$_3$N$_4$-B heterojunction with larger contact area and active sites. Further, its potential for catalytic reduction of RhB and methylene blue (MB) under visible light has been assessed.

EXPERIMENT

1. Materials

Melamine (Macklin, 99%), Bi (NO$_3$)$_3$·5H$_2$O (Sinoreagent, AR), NaH$_2$PO$_4$ (McLean, 99.9%) boric acid (Macklin, GR), NaCl (Sino-

reagent, AR), rhodamine B (Beijing reagent, AR), methylene blue (McLean, AR), acetic acid (Sinoreagent, AR), deionized water (homemade), and ethanol (Sinoreagent, AR) were used in this work without any further purification.

2. Synthetic Procedure

g-C$_3$N$_4$-B was prepared via calcination at a high temperature. Briefly, 1.0 g of melamine, 1.0 g of boric acid, and 1.0 g of NaCl [18], were put into an agate mortar for full grinding and mixing. The obtained ground powder was dissolved in 30 mL of anhydrous ethanol, heated, stirred, and evaporated to dry most of the ethanol at 80 °C. Then it was kept in an oven to dry completely. The dried mixture was again ground into powder, placed in a covered crucible, and calcined in a muffle furnace at 550 °C for 4 h (Direct calcination without programmed temperature). The crucible was taken out after natural cooling to room temperature, and the obtained yellow product after calcination was ground in an agate mortar to obtain g-C$_3$N$_4$-B.

A coprecipitation technique was adopted to prepare BiPO$_4$/g-C$_3$N$_4$-B. Briefly, 0.4851 g of Bi (NO$_3$)$_3$·5H$_2$O and different masses of g-C$_3$N$_4$-B (0.0920 g, 0.1840 g, 0.2760 g) were added into 20 mL of acetic acid and ultrasonicated for 10 min. Separately, 0.1198 g of NaH$_2$PO$_4$ was added into 20 mL of deionized water. The two aforementioned systems were stirred for 20 min and then mixed. The stirring was further continued for 1 h, and then the mixture was centrifuged. The obtained precipitate was washed alternately with deionized water and anhydrous ethanol, then put into an oven at 60 °C for 6 h to dry it, and then ground to obtain the composites. Composites with BiPO$_4$: g-C$_3$N$_4$-B mass ratios of 1 : 1, 1 : 2, and 1 : 3 were marked as 1 : 1BP-CB, 1 : 2BP-CB, and 1 : 3BP-CB, respectively. Additionally, pure BiPO$_4$ was prepared via the same method, except that the mass of g-C$_3$N$_4$-B was 0 in that case.

3. Photocatalytic Experiment

The target pollutants for photocatalytic experiments to evaluate the photocatalytic activity of different samples were RhB and MB dyes. Briefly, 50 mg of the sample was dispersed into a reaction flask containing 50 mL of dye (10 mg/L) and stirred for 1 h under dark conditions to achieve adsorption-desorption equilibrium. Then,

an LED lamp was used to irradiate the reaction bottle, aliquots were taken out from the reaction mixture at different times, and the absorbance was measured after centrifugation.

4. Sample Characterization

The X-Ray diffraction (XRD) patterns were obtained for characterizing the bulk phase structure of the prepared samples, using a Cu K$_\alpha$ radiation X-ray diffractometer (Rigaku Ultima IV, Japan) at a scanning range of 5°-90°, a scanning rate of 8° min^{-1}, a voltage of 40 kV and a current of 40 mA. The microscopic morphology of the samples was investigated using FEI Inspect F50 field emission scanning electron microscope (SEM), and energy dispersal spectroscopy (EDS) was done for the composite material. The distribution of the chemical composition of the prepared sample was also studied by EDAX super octane using the same instrument. The internal lattice structure of the sample was observed using a Talos F200S G2 high-resolution transmission electron microscope (HR-TEM). A lambda 1050 UV-vis near-infrared spectrophotometer was used to obtain the UV-vis diffuse reflectance spectra (UV-vis DRS) of the sample in the range of 200-800 nm with BaSO$_4$ as the standard. The chemical state of the elements on the surface of the sample was probed through an X-ray photoelectron spectrometer (XPS, ThermoFisher, ESCALAB Xi+) using Al K$_\alpha$ radiation. A PL-SPV/IPCE1000 stable surface photovoltage spectrometer (Beijing Poffile Technology Co., Ltd.) was used to obtain the surface photovoltage (SPV) spectrum of the sample. A CS310H electrochemical workstation with a standard three-electrode system was used to measure the electrochemical impedance spectroscopy (EIS) and transient photocurrent response of the samples (irradiated by a 300 W xenon lamp). A Thermofly Escalab Xi+ instrument was used to measure the ultraviolet photoelectron spectroscopy (UPS) of the samples.

RESULTS AND DISCUSSION

1. XRD Study

Fig. 1 depicts the XRD patterns of the pure BiPO$_4$ and BP-CB composites with different proportions. The diffraction peaks of
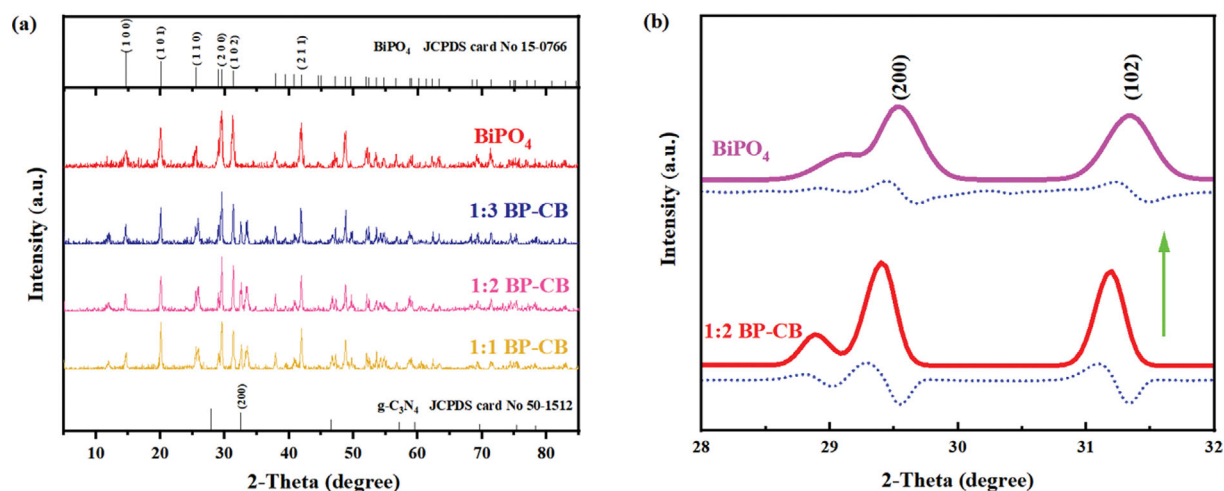

Fig. 1. (a) XRD spectra of BiPO$_4$, 1 : 1BP-CB, 1 : 2BP-CB, and 1 : 3BP-CB and (b) The amplification of Bragg peaks (200) and (102) in the range of 28-32°.
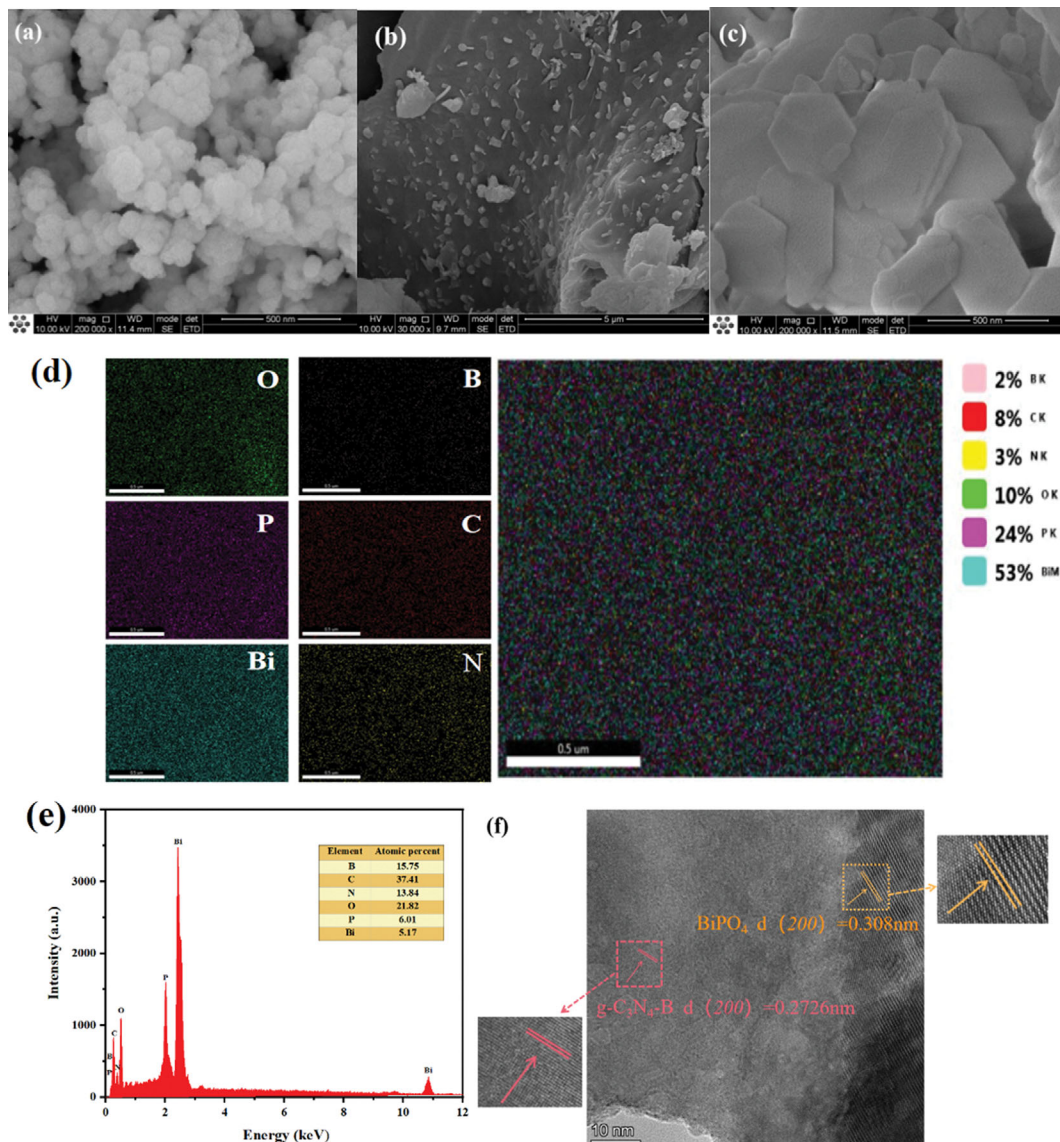
Fig. 2. SEM images of BiPO₄ (a), g-C₃N₄-B (b), and 1 : 2BP-CB (c); element map (d), EDS map (e), and HR-TEM map (f) of 1 : 2BP-CB.

pure BiPO₄ at 2θ values of 14.6°, 20.1°, 25.5°, 29.5°, 31.3°, 41.9°, and 49.6° were evident, which was attributed to the (100), (101), (110), (200), (102), (211), and (113) crystal planes of hexagonal BiPO₄, respectively (JCPDS 15-0766). Although the XRD patterns of the BP-CB composites with different proportions mainly represent the characteristic diffraction peaks of BiPO₄, a different peak was found at 2θ value of 32.5°, which corresponded to the (200) crystal plane of g-C₃N₄ (JCPDS 50-1512). Fig. 1(b) shows the amplification of Bragg peaks (200) and (102) in the range of 28-32°, The solid line represents the experimental data of using Jade for Rietveld refinement, and the dashed line is the difference between experimental data and refined experimental data. Obviously, compared to BiPO₄, the (200) and (102) Bragg peaks of 1 : 2BP-CB are significantly enhanced and narrowed, which explains why the composite material 1 : 2BP-CB still maintains a planar sheet shape (Fig. 2(c)) [19].

2. SEM and HRTEM Studies

The photocatalytic activity of a material depends considerably

on its morphology; therefore, the morphology and microstructure of the prepared materials were characterized using SEM, EDS, and HRTEM. Fig. 2(a) displays the SEM image of pure BiPO₄, where small round chips of 50-100 nm, stacked together one by one, are evident. On the other hand, g-C₃N₄-B has an irregular sheet-like morphology (Fig. 2(b)). Fig. 2(c) suggests that the 1 : 2BP-CB heterojunction has a 200-500 nm nanoflake-like morphology. Notably, the morphology of the composite 1 : 2BP-CB is very much different from that of pure BiPO₄ and g-C₃N₄-B counterparts. It could be speculated that during the synthesis of BiPO₄, there is no interference from other substances around Bi³⁺ after adding NaH₂PO₄, so BiPO₄ forms rapidly and stacks into small chips. However, during the formation of composite 1 : 2BP-CB material, g-C₃N₄-B nanosheets (stripped by the acetic acid solution of bismuth nitrate pentahydrate under ultrasonic conditions) surround Bi³⁺. Therefore, soon after the addition of NaH₂PO₄, the rapidly generated BiPO₄ attaches to the surface of the g-C₃N₄-B nano-sheets, forming 2D/
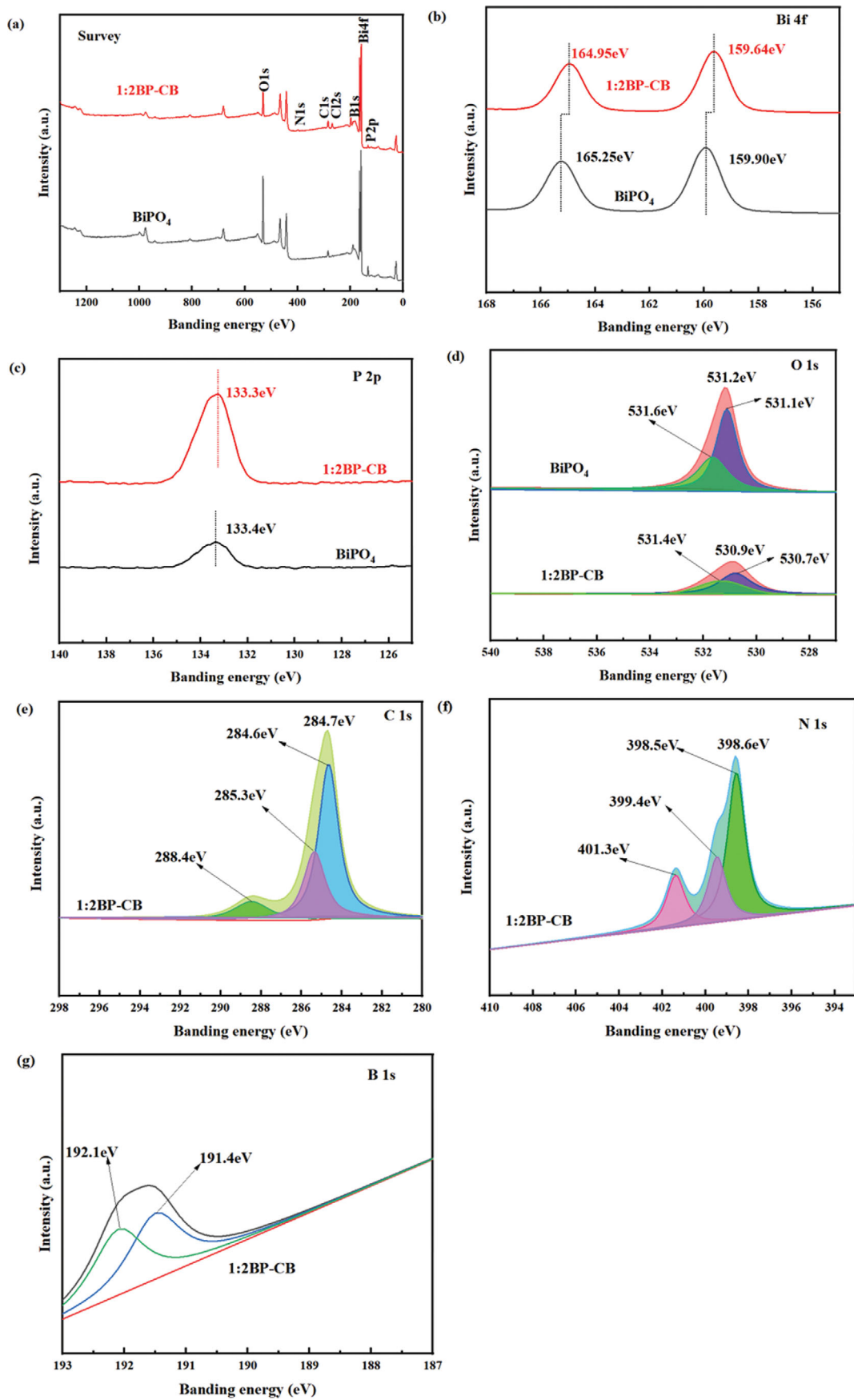
Fig. 3. XPS spectra of the samples.

2D BiPO$_4$/g-C$_3$N$_4$-B heterostructure. At the same time, the contact area of g-C$_3$N$_4$-B and BiPO$_4$ is increased, the aggregation of catalyst particles is improved, and more surface reaction sites are provided after the formation of BiPO$_4$/g-C$_3$N$_4$-B catalyst with 2D/2D morphology, which further improves its photocatalytic activity [20].

The elemental mapping (Fig. 2(d)) confirms the existence of C, N, O, P, B, and Bi in the 1 : 2BP-CB heterojunction, and each element is evenly distributed in the complex. Additionally, the EDS diagram (Fig. 2(e)) also shows that 1 : 2BP-CB was composed of C, N, O, P, B, and Bi elements. The HRTEM image (Fig. 2(f)) displays the crystalline structure of 1 : 2BP-CB, and a clear boundary between two different lattices is observed, indicating the existence of high-density atomic defects [21]. The lattice spacings of 0.308 nm and 0.273 nm were concluded, corresponding to the (200) crystal planes of BiPO$_4$ and g-C$_3$N$_4$-B, respectively, which is consistent with the lattice spacing shown on the PDF standard card of XRD. All the aforementioned characterization collectively confirm the successful synthesis of 2D/2D BiPO$_4$ nano-sheet/g-C$_3$N$_4$-B nano-sheet heterojunction.

3. XPS Study

Fig. 3 depicts the XPS spectra of the samples. The full spectra of pure BiPO$_4$ and 1 : 2BP-CB composites are displayed in Fig. 3(a). The existence of P, Bi, B, C, N, and O elements in the 1 : 2BP-CB composite is evident. The peaks at 191.6 eV, 284.7 eV, and 398.6 eV correspond to B1s, C1s, and N1s bands in the composites, respectively. The high-resolution spectrum of Bi 4f (Fig. 3(b)) shows that the characteristic peaks of Bi4f$_{7/2}$ and Bi4f$_{5/2}$ in BiPO$_4$ are at 165.25 eV and 159.90 eV, respectively, whereas they move slightly to lower binding energy (164.95 eV and 159.64 eV, respectively), in the case of 1 : 2BP-CB heterojunction [22]. Fig. 3(c) depicts the high-resolution XPS diagram of P 2p. A similar peak at 133.4 eV and 133.3 eV for BiPO$_4$ and 1 : 2BP-CB, respectively, indicates that the phosphorus element is present in the oxidation state of +5 in both these materials [23]. Moreover, the intensity of the P 2p peak of the 1 : 2BP-CB composite is much higher than that of pure BiPO$_4$, indicating the change in the chemical environment around phosphorus. Fig. 3(d) shows the high-resolution XPS diagram of O 1s, where the peak of pure BiPO$_4$ at 531.6 eV is attributed to adsorbed oxygen, while the peak at 531.1 eV corresponds to lattice oxygen [24]. Notably, the peaks for adsorbed oxygen and lattice oxygen of 1 : 2BP-CB are shifted toward reduced binding energy and are located at 531.4 eV and 530.7 eV, respectively. The C 1s high-resolution XPS diagram (Fig. 3(e)) of 1 : 2BP-CB heterojunction exhib-
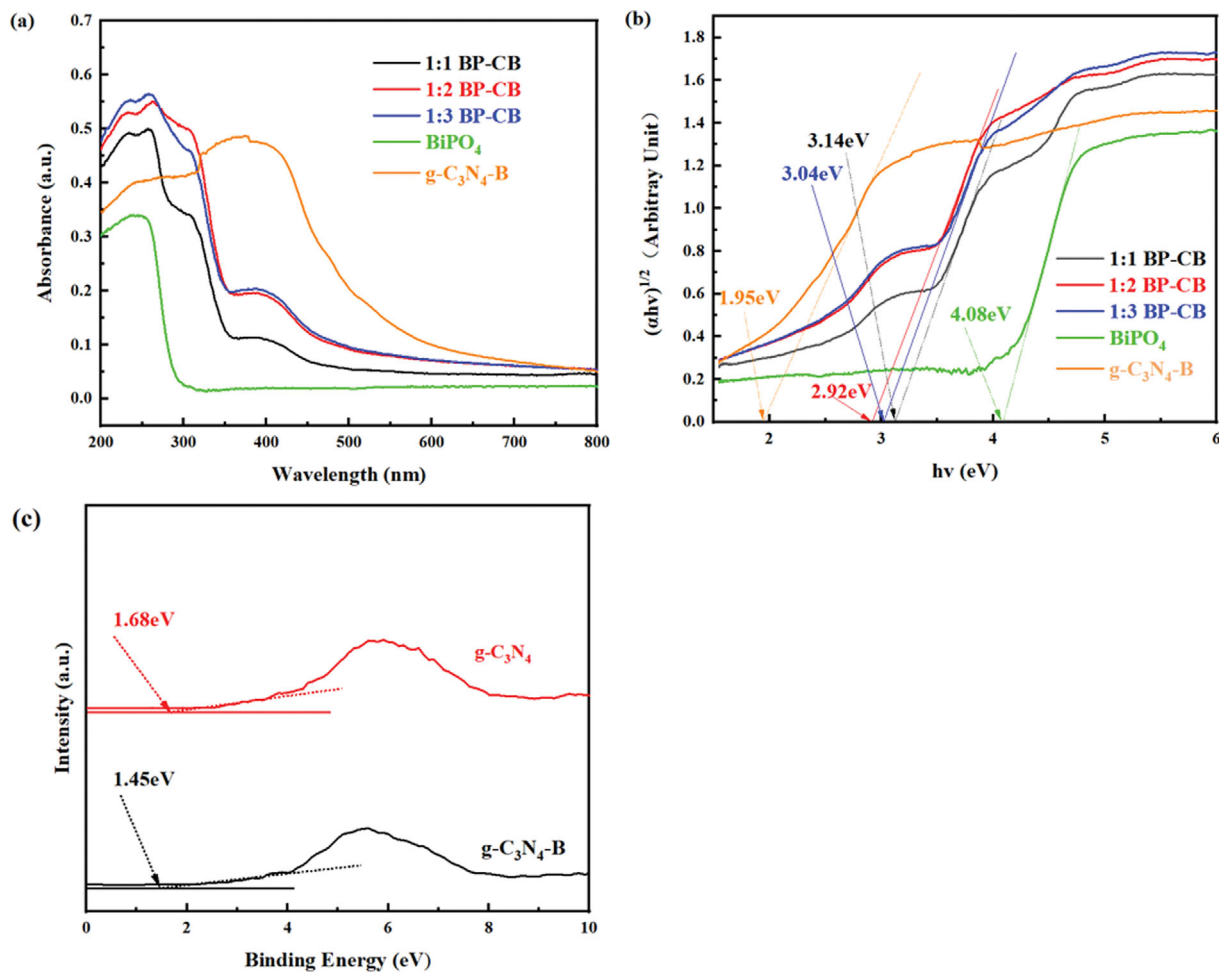

Fig. 4. (a) UV-vis DRS spectra and (b) Tauc diagrams of g-C$_3$N$_4$-B, BiPO$_4$, and BP-CB in different proportions; (c) XPS VBs spectra of g-C$_3$N$_4$-B and g-C$_3$N$_4$.

its a peak at 284.6 eV, representing the C-C peak of the sample, while the peak at 288.4 eV is attributed to the sp2 hybridized carbon (N-C≡N), and the peak at 285.3 eV belongs to the adsorbed carbon [25]. Fig. 3(f) shows the high-resolution XPS spectra of N 1s, where the characteristic peaks of pyridine nitrogen (C-N=C), graphite nitrogen (C-N), and pyrrolidine nitrogen (C-N-H) of 1 : 2BP-CB composite appear at 398.5 eV, 399.4 eV, and 401.3 eV binding energies, respectively [26]. Fig. 3(g) depicts the B 1s spectrum of 1 : 2BP-CB heterojunction, where the peaks at 192.1 eV and 191.4 eV correspond to B-(N)$_3$ and -N$_2$BH, respectively [17]. The changes in the chemical environment around Bi, P, and O elements in the 2D/2D composite heterostructure compared to the individual counterparts indicate that there is a strong chemical bond between the g-C₃N₄-B nano-sheet and the BiPO₄ nano-sheet.

4. DRS and VBs Spectral Studies

The optical properties of a material must be investigated for its photocatalysis applications. Here, the optical absorption performance and band gap of the prepared samples were determined using UV-vis DRS spectra (Fig. 4(a)), which represented the light response of the sample in the wavelength range of 200-800 nm. The results suggest that the absorption edge of the pure BiPO₄ was about 310 nm, while the absorption edge of the composite BP-CB

material shifted toward the longer wavelengths (redshifted to 390-430 nm). This indicates that the combination with g-C₃N₄-B could broaden the absorption range of BiPO₄ and effectively promote the absorption of visible light to enhance the photocatalytic activity.

Fig. 4(b) represents the Tauc plot of the prepared material, which is a typical (αhv)$^{1/2}$-hv linear plot. Notably, as BiPO₄ and BiPO₄/C₃N₄ are indirect semiconductors, here, the index of αhv was taken as 1/2. The standard calculations from the Tauc plots concluded E$_g$ values of 1.95 eV, 4.08 eV, 3.14 eV, 2.92 eV, and 3.04 eV for g-C₃N₄-B, BiPO₄, 1 : 1BP-CB, 1 : 2BP-CB, and 1 : 3BP-CB, respectively. The band gap of the composite decreased first and then increased with the increase in the g-C₃N₄-B content of the composite. Notably, the band gap of 1 : 2BP-CB was the smallest, but the absorption range of light was the largest.

Additionally, the band edge positions of BiPO₄ could be estimated using the following empirical formulas:

$$E_{VB} = X - E_e + 0.5E_g$$
$$E_{CB} = E_{VB} - E_g$$

where E$_{VB}$ is the edge potential of the valence band (VB), E$_{CB}$ is the edge potential of the conduction band (CB), X is the average electronegativity of the semiconductor (the value of BiPO₄ is 6.49)
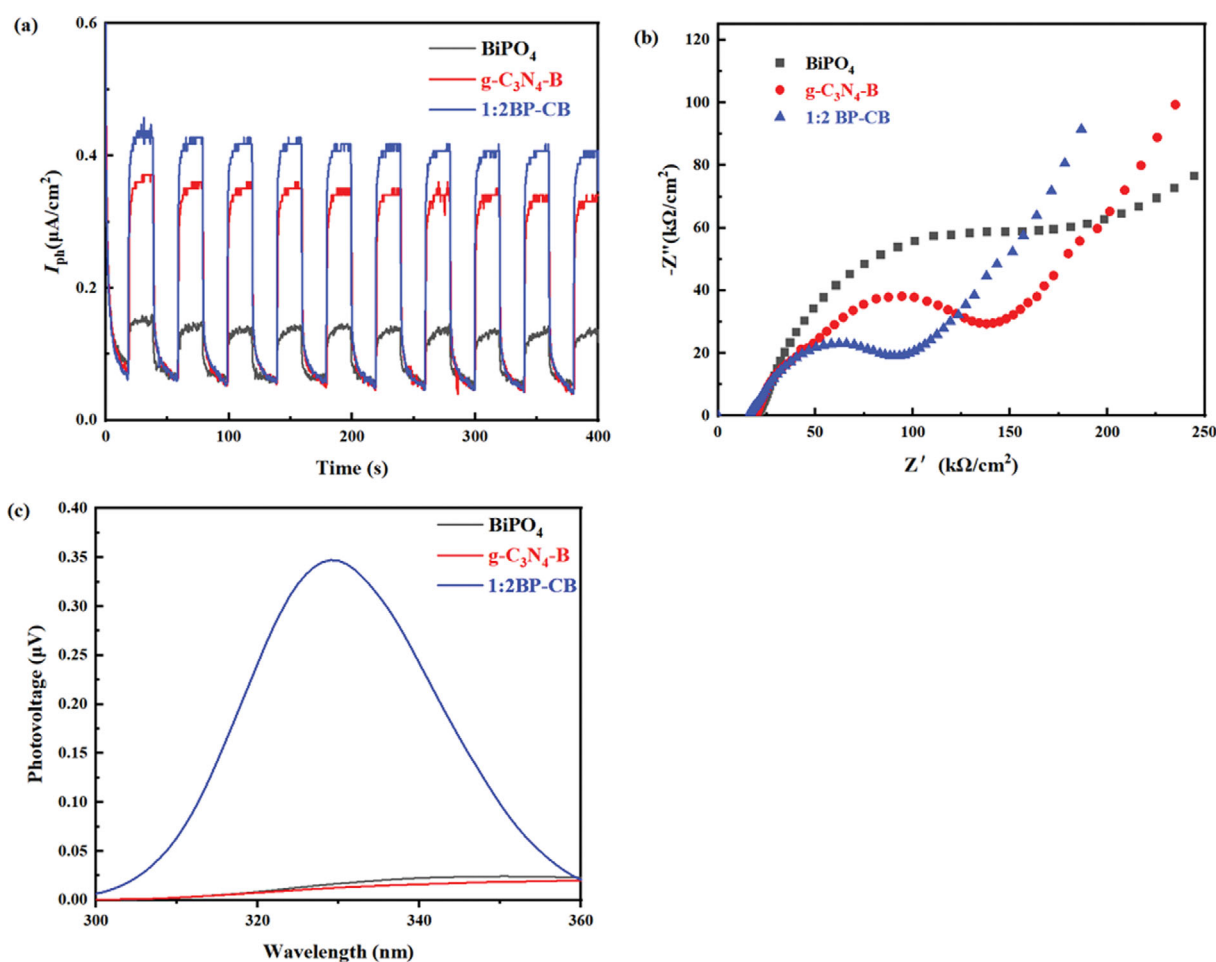

Fig. 5. (a) Transient photocurrent, (b) EIS diagram, and (c) SPV diagram of BiPO₄, g-C₃N₄-B, and 1 : 2BP-CB for their electrochemical characterization.

[27], E_e is the free electron energy on the hydrogen scale (about 4.5 eV), and E_g is the band gap of the semiconductor. The E_{VB} and E_{CB} values of BiPO$_4$ were found to be 4.03 eV and −0.05 eV, respectively. Now, g-C$_3$N$_4$-B, due to the incorporation of B, the X value cannot be the same as the known X value of g-C$_3$N$_4$. Therefore, the g-C$_3$N$_4$-B sample was characterized using their XPS VBs spectra (Fig. 4(c)), which concluded the E_{VB} value of 1.45 eV for g-C$_3$N$_4$-B. The E_{CB} was then calculated to be −0.50 eV.

5. Transient Photocurrent, EIS, and SPV Studies

The transient photocurrent response curves (Fig. 5(a)) indicate that all samples could produce fast and stable photocurrent signals under visible light irradiation with periodic changes while passing through 10 intermittent switches. The photocurrent of the samples increased rapidly when it was illuminated and then decreased rapidly upon the withdrawal of the illumination. Notably, the photocurrent intensity of 1 : 2BP-CB was the highest. This indicates
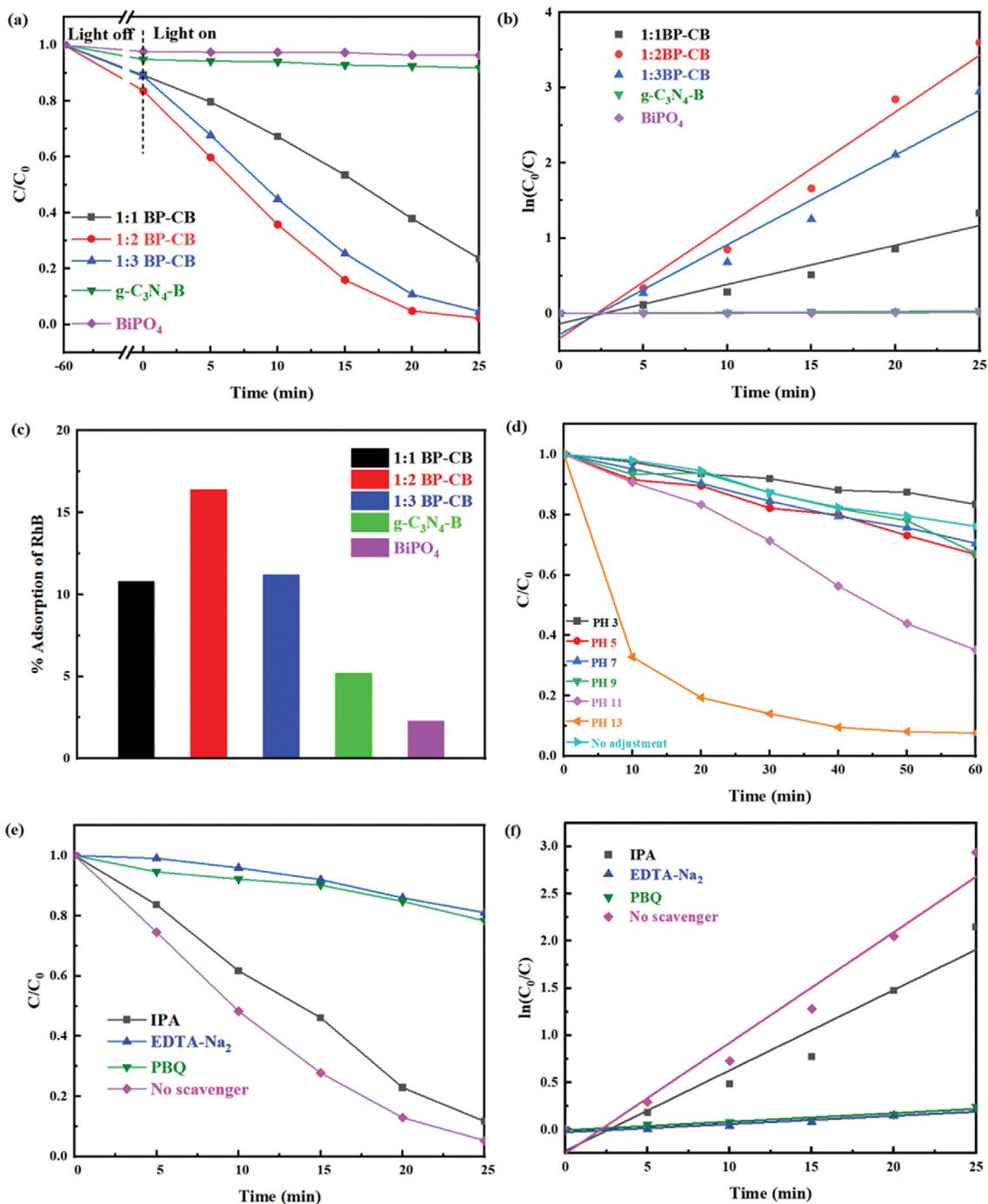

Fig. 6. (a) The photocatalytic degradation effect and (b) degradation kinetics of RhB; (c) The adsorption rate of RhB on the sample; (d) Degradation effect of 1 : 2BP-CB on MB at different pH values; (e) Photocatalytic performance and (f) degradation kinetics of 1 : 2BP-CB to RhB under the presence of different inactivators.

Table 1. Comparison of photocatalytic activities of BiPO$_4$ based composites toward the degradation of RhB

Combined material	Method	Catalyst quality	Concentration/ volume of RhB	Degradation time/ rate	Light	References
Bi-BiOBr/BiPO$_4$	Hydrothermal	50 mg	10 mg/L/100 ml	90 min/89.7%	Xenon lamp, 350 W	[8]
Fe$_3$O$_4$/BiPO$_4$	Hydrothermal	250 mg	5 mg/L/250 ml	360 min/92%	UV-lamp, 9 W	[9]
CQDs/Ag$_3$PO$_4$/BiPO$_4$	Hydrothermal	100 mg	5 mg/L/100 ml	50 min/98.7%	Xenon lamp, 200 W	[10]
BiPO$_4$/Bi$_2$O$_2$CO$_3$	Hydrothermal	100 mg	5 mg/L/200 ml	40 min/92.6%	Mercury lamp, 300 W	[11]
BiPO$_4$/Bi$_4$O$_5$I$_2$	Hydrolysis	10 mg	20 mg/L/50 ml	120 min/93%	UV-light	[12]
BiPO$_4$/g-C$_3$N$_4$-B	Co-precipitation	50 mg	10 mg/L/50 ml	25 min/97.3%	LED lamp, 5 W	This work

that the combination of g-C$_3$N$_4$-B and BiPO$_4$ improved the separation of photogenerated electrons and holes [28]. Additionally, EIS (Fig. 5(b)) was also used to study the charge transfer behavior of these samples. The 1:2BP-CB sample had the smallest arc radius, so it showed a smaller resistance value and faster charge transfer capability [29]. It may be noted that a certain voltage will be generated when the electrons are transferred from the VB to the CB. According to previous reports, the intensity of SPV optical voltage can explain the separation efficiency of electron-hole pairs [30]. The SPV diagrams of the combined samples are depicted in Fig. 5(c). The g-C$_3$N$_4$-B and 1:2BP-CB samples showe higher voltage and photogenerated carrier separation efficiency compared to pure BiPO$_4$. The aforementioned results of transient photocurrent response, EIS, and SPV analysis show that the combination of g-C$_3$N$_4$-B and BiPO$_4$ significantly enhanced the separation and transfer efficiency of photogenerated carriers in the 1:2BP-CB heterojunction.

6. Photocatalytic Activity

The photocatalytic degradation of RhB in the presence of different samples under visible light irradiation is shown in Fig. 6(a). Pure BiPO$_4$ and g-C$_3$N$_4$-B exhibit almost negligible photodegradation effects on RhB, whereas the degradation rate is significantly improved in the presence of the BP-CB composites. Notably, 1:2BP-CB shows the best degradation rate of RhB, reaching 97.3% photodegradation in only 25 min.

Fig. 6(b) illustrates the first-order kinetic curves of RhB photodegradation in the presence of different samples, which concluded rate constants of 0.0005803 min^{-1}, 0.00132 min^{-1}, 0.0521 min^{-1}, 0.1505 min^{-1}, and 0.1191 min^{-1}, for BiPO$_4$, g-C$_3$N$_4$-B, 1:1BP-CB, 1:2BP-CB, and 1:3BP-CB, respectively. The degradation rate is the fastest in the presence of 1:2BP-CB, which is 259.3 and 114.0 times faster than that of pure BiPO$_4$ and pure g-C$_3$N$_4$-B, respectively, indicating the significant enhancement of photocatalytic RhB degradation activity after the formation of heterojunction.

Additionally, the adsorption rates of RhB by different samples while keeping the reaction mixture in the dark for 1 h (before light irradiation) are depicted in Fig. 6(c). Although g-C$_3$N$_4$-B and RhB had poor adsorption effects, the adsorption performance of the BP-CB composite improved. Here, 1:2BP-CB exhibits the best adsorption rate, which is 7.13 times more than that of BiPO$_4$.

It can be concluded, based on the above photocatalytic degradation experiments and results of the sample characterization, that the 1:2BP-CB sample (synthesized via the combination of BiPO$_4$ and g-C$_3$N$_4$-B) has the highest dye adsorption performance, the highest photogenerated charge-hole separation efficiency, and greatly

improved absorption of visible light. These results in its superior photocatalytic degradation performance.

Furthermore, the photocatalytic RhB degradation performance of semiconductors related to BiPO$_4$ in recent years was extracted from the literature and summarized in Table 1.

However, 1:2 BP-CB could not significantly photodegrade MB. If the pH is not adjusted, the degradation of MB is relatively slow, and complete degradation js in about 200 minutes. The MB degradation efficiency of the 1:2 BP-CB sample at different solution pH values of 1, 3, 5, 7, 9, 11, and 13 is shown in Fig. 6(d). The degradation effect on MB exhibits some improvement at pH 11, while it reaches its best upon further increasing the pH of the MB solution to 13. It degrades MB completely in only 40 min under these conditions. It is speculated that the reason for the pH dependence is that when pH is equal to 11, beyond the isoelectric point of 1:2BP-CB, 1:2BP-CB begins to change into a negatively charged surface, thus increasing the electrostatic attraction with the MB (cationic dye) [31]. Therefore alkaline conditions are favorable for the degradation of MB by the BP-CB complex.

It is necessary to determine the main active species involved in the process of photocatalytic degradation to further clarify the mechanism of photocatalysis of the BP-CB composite material. Therefore, free radical capture experiments were performed for the composite material 1:2BP-CB. Figs. 6(e) and (f) show that the degradation of RhB by 1:2BP-CB was greatly inhibited after the addition of p-benzoquinone (PBQ, •O$_2^-$ scavenger) and ethylenediaminetetraacetic acid disodium salt (Na$_2$EDTA, h$^+$ scavenger). This indicates that •O$_2^-$ and h$^+$ play a major role in the degradation of RhB. However, the photodegradation rate of RhB in the presence of isopropanol (IPA, •OH scavenger) decreased slightly only, which indicates that •OH also plays a role in the degradation of RhB.

7. Proposed Mechanism

A plausible mechanism for photocatalytic RhB degradation by BP-CB composites is proposed in Fig. 7(a). Upon irradiation of BP-CP composites with LED light, the photogenerated electrons (e$^-$) on g-C$_3$N$_4$-B and BiPO$_4$ jump to their respective CB and left holes (h$^+$) on their VB. Now, the electrons in the g-C$_3$N$_4$-B CB are transferred to the CB of BiPO$_4$, and the holes in the VB of BiPO$_4$ are transferred to the VB of g-C$_3$N$_4$-B. However, as the potential of the BiPO$_4$ CB (−0.05 eV) is more positive than the redox potential of O$_2$/•O$_2^-$ (−0.33 eV), the electrons of the BiPO$_4$ CB are unable to reduce the O$_2$ adsorbed on BiPO$_4$ to •O$_2^-$. Moreover, the g-C$_3$N$_4$-B VB potential value (1.45 eV) is lower than the redox potential of •OH/H$_2$O (2.68 eV), and the holes accumulated in the g-C$_3$N$_4$-B

(a)

(b)

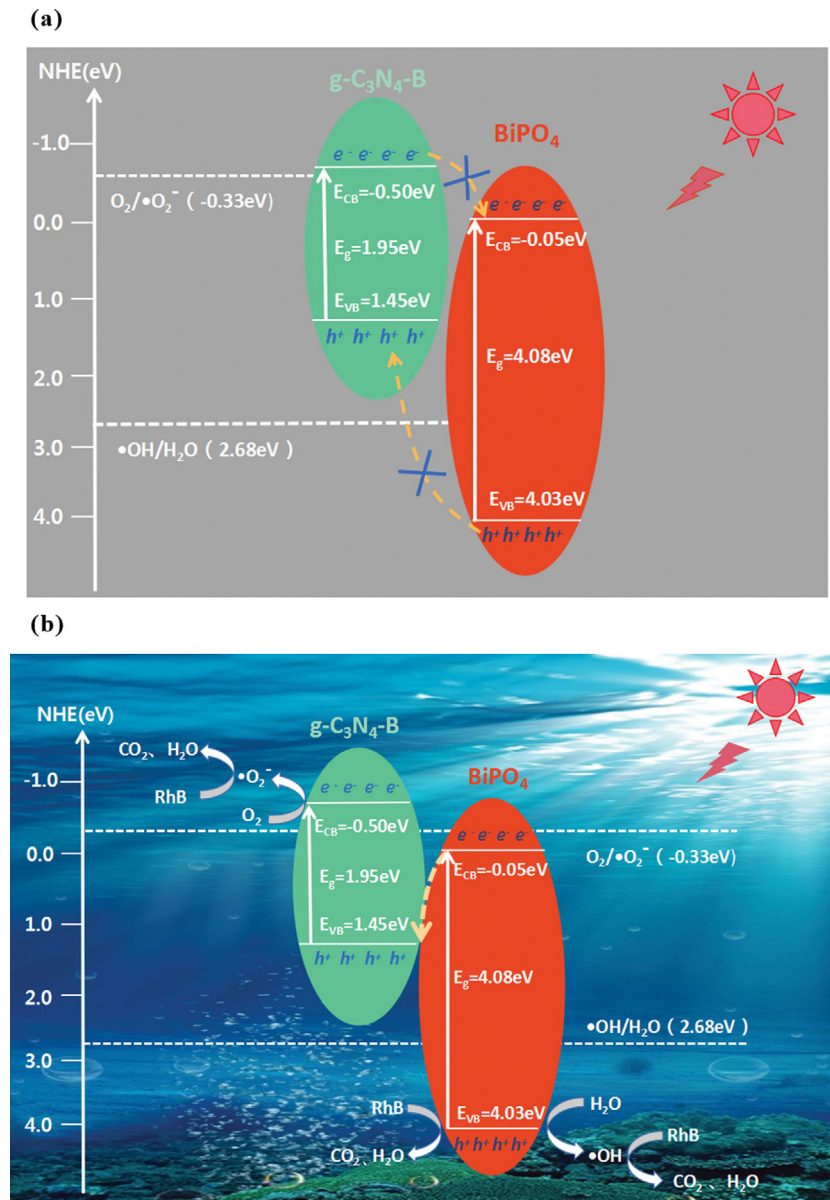**Fig. 7. Proposed mechanisms for photogenerated charge transfer and photocatalysis on the surface of the composite.**

VB could not oxidize H_2O to •OH [32]. This is inconsistent with the results of free radical trapping experiments. Therefore, the traditional photoexcited carrier transfer and charge separation in a type II heterojunction is not suitable for the BP-CP composites [33,34].

Therefore, an alternate mechanism is proposed in Fig. 7(b). Upon illumination of BP-CB by the LED lamp, electrons on the surface of g-C_3N_4-B and $BiPO_4$ are photoexcited, and electrons (e^-) and holes (h^+) are generated in their CB and VB, respectively. Next, the electrons in the CB of $BiPO_4$ and the holes in the VB of g-C_3N_4-B are quenched together [35], which ultimately concentrates electrons in the CB of g-C_3N_4-B and holes in the VB of $BiPO_4$. As the potential of the CB of g-C_3N_4-B is −0.50 eV, these photoelectrons can reduce the O_2 adsorbed on g-C_3N_4-B to •O_2^-. On the other hand, the high VB potential of 4.03 eV of $BiPO_4$ empowered the holes with strong oxidation ability and oxidizes H_2O on the sur-

face of $BiPO_4$ to generate •OH. This is consistent with the results of the free radical capture experiment. Therefore, the $BiPO_4$/g-C_3N_4-B composite synthesized by this strategy must be a direct Z-type heterojunction photocatalyst.

The exactness of the speculated hypothesis proposed above was verified using the work function values. The E_{Cutoff} of the samples could be obtained from Fig. 8 when the abscissa was the binding energy.

Now, the following formula [36] was used to calculate the work function (Φ) of the samples:

$$\Phi = h\nu - (E_{Cutoff} - E_{Fermi})$$

Here, E_{Cutoff} was the abscissa value corresponding to the intersection of the tangent of the secondary electron cut-off edge and the baseline, and E_{Fermi} is the abscissa value corresponding to the mid-
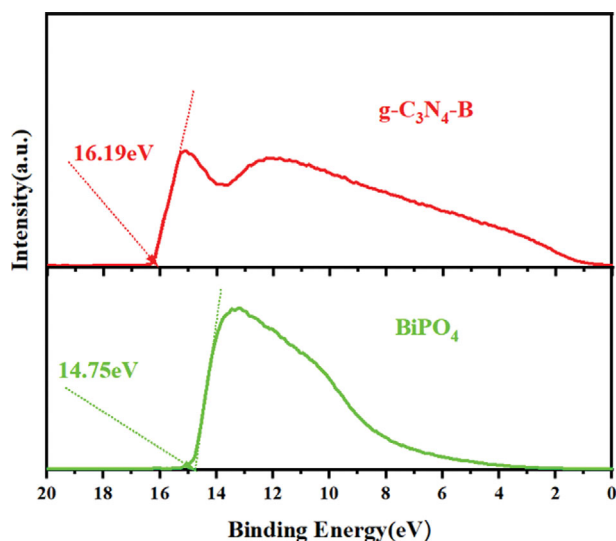
Fig. 8. E$_{Cutoff}$ of sample.

point of the Fermi boundary curve [37]. The photon energy hν was 21.22 eV in all cases. Therefore,

$$\Phi_{\text{g-C3N4-B}}=21.22\,\text{eV}-(16.19\,\text{eV}-0)=5.12\,\text{eV}$$
$$\Phi_{\text{BiPO4}}=21.22\,\text{eV}-(14.75\,\text{eV}-0)=6.47\,\text{eV}$$
$$E_F=\Phi-E_{ac}$$

where E$_F$ is Fermi energy level, Φ is the work function, and E$_{ac}$= 4.5 eV(the difference between the vacuum level and the standard hydrogen electrode).

The energy band configuration diagram of BP-CB could be drawn according to the above calculation results [38]. Here, both the semiconductor photocatalysts have staggered energy band structures and different Fermi energy levels (Fig. 9(a)). Therefore, upon bringing them in contact with each other (Fig. 9(b)), the difference in the work function between them induces the free electrons of g-C₃N₄-B to migrate to BiPO₄, the energy band at the contact site bends, and the charge is redistributed until the Fermi energy level reaches equilibrium. This forms an internal electric field [39]. This energy band bending at the interface of the heterojunction simultaneously inhibits the transfer of electrons in the g-C₃N₄-B CB to

the BiPO₄ CB and the transfer of holes in the BiPO₄ VB to the g-C₃N₄-B VB. This, in turn, promotes the recombination of electrons in the BiPO₄ CB with holes in the g-C₃N₄-B VB [37], forming a direct Z-type heterojunction. This corroborated well with the proposed photocatalysis mechanism shown in Fig. 7(b). Therefore, the abrupt change of energy band structure at the interface of BiPO₄/ g-C₃N₄-B heterojunction resulted in the bending of its energy band and the formation of an internal dielectric field. Effective separation of carriers at the interface was promoted in this direct Z-type heterojunction, and an enhanced oxidation-reduction ability was also found simultaneously. Furthermore, semiconductor materials BiPO₄ and g-C₃N₄-B could easily be assembled into 2D/2D BiPO₄/ g-C₃N₄-B nanochips to achieve an effective combination of different multi-functional materials. Therefore, this work suggests that the 2D/2D BiPO₄/g-C₃N₄-B direct Z-type heterojunction has a considerable potential from the perspective of a broader photocatalytic application.

CONCLUSION

A 2D/2D BiPO₄/g-C₃N₄-B nano-sheet heterojunction was designed via the epitaxial growth of BiPO₄ on g-C₃N₄-B to obtain a broadened absorption spectrum and improved separation efficiency of photogenerated electron-hole pairs. It was further applied as a photocatalyst for the degradation of dyes such as RhB and MB in water. The dye degradation experiments showed that the photocatalytic degradation efficiency was greatly improved for the heterojunction comprising g-C₃N₄-B and BiPO₄, compared to the individual constituents. The experimental results of SPV, EIS, instantaneous current response, free radical capture, UPS, and DRS comprehensively concluded that the efficient photocatalytic effect of 2D/2D BiPO₄/g-C₃N₄-B complex originated mainly from its highly improved visible light absorption performance and the enhanced separation efficiency of electron-hole pairs in this direct Z-type heterostructure.
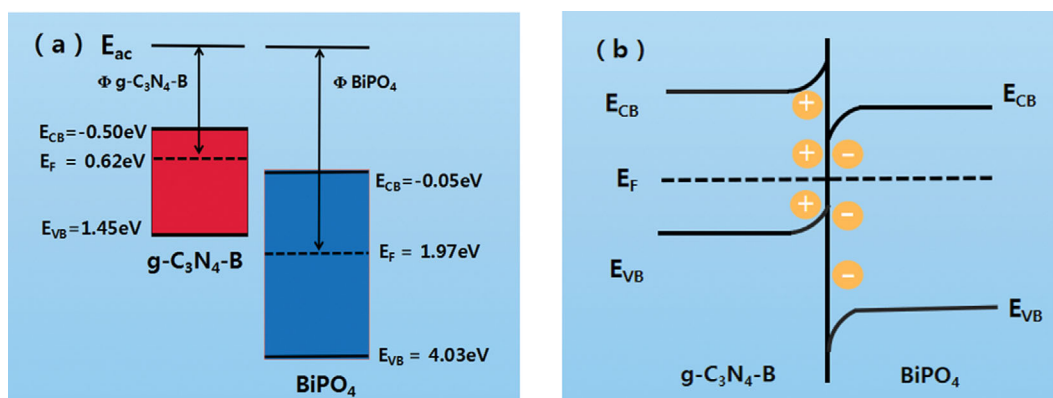
ACKNOWLEDGEMENTS

Fig. 9. Schematic diagram of semiconductors with staggered energy band configuration: (a) Before contact, and (b) after contact.

REFERENCES

1. J. C. Medina, M. Bizarro, P. Silva-Bermudez, M. Giorcelli, A. Tagliaferro and S. E. Rodil, *Thin. Solid. Films.*, **612**, 72 (2016).
2. J. Xie, Y. L. Cao and D. Z. Jia, *J. Alloys. Compd.*, **832**, 154953 (2020).
3. N. A. Mohamed, J. Safaei, A. F. Ismail, M. N. Khalid, M. F. A. Mohd Jailani, M. F. M. Noh, N. A. Arzaee, D. Zhou, J. S. Sagu and M. A. M. Teridi, *Mater. Res. Bull.*, **125**, 110779 (2020).
4. J. Shokraiyan, V. Jahed and M. Rabbani, *J. Chin. Chem. Soc.*, **68**, 1880 (2021).
5. G. J. Guo, and H. Yan, *Chem. Phys.*, **538**, 110920 (2020).
6. R. Kumar, P. Raizada, A. A. P. Khan, V. H. Nguyen, Q. Van Le, S. Ghotekar, R. Selvasembian, V. Gandhi, A. Singh and P. Singh, *J. Mater. Sci. Technol.*, **108**, 208 (2022).
7. Y. Naciri, A. Hsini, Z. Ajmal, J. A. Navio, B. Bakiz, A. Albourine, M. Ezahri and A. Benlhachemi, *Adv. Colloid. Interface. Sci.*, **280**, 102160 (2020).
8. C. B. Wu, C. X. Zhou, Y. Y. Chen, Z. G. Peng, J. Yang and Y. M. Zhang, *J. Nanomater.*, **2021**, 1 (2021).
9. Y. Chen, X. L. Jin and P. Guo, *J. Mol. Struct.*, **1171**, 140 (2018).
10. H. J. Gao, C. X. Zheng, H. Yang, X. W. Niu and S. F. Wang, *Micromachines*, **10**, 557 (2019).
11. Y. M. Liu, P. Zhang, H. Lv, J. Guang, S. Li and J. H. Jiang, *RSC Adv.*, **5**, 83764 (2015).
12. X. Zhang, P. Yang, B. Yang, Y. Bai, W. H. Liu, H. B. Huo, J. M. Li and G. Li, *New. J. Chem.*, **45**, 18957 (2021).
13. W. Q. Kong, X. F. Zhang, B. B. Chang, Y. N. Zhou, S. R. Zhang, G. L. He, B. C. Yang and J. J. Li, *Electrochim. Acta*, **282**, 767 (2018).
14. G. Q. Tan, L. N. She, T. Liu, C. Xu, H. J. Ren and A. Xia, *Appl. Catal. B*, **207**, 120 (2017).
15. X. J. Zou, Y. Y. Dong, Z. B. Chen, D. P. Dong, D. X. Hu, X. Y. Li and Y. B. Cui, *RSC Adv.*, **6**, 20664 (2016).
16. J. Jang Ng, K. Hon Leong, L. Ching Sim, Y. Heng Chin and S. Pichiah, *MSE*, **917**, 012007 (2020).
17. W. K. Wang, H. J. Zhou, Y. Y. Liu, S. B. Zhang, Y. X. Zhang, G. Z. Wang, H. M. Zhang and H. J. Zhao, *Small*, **16**, 1906880 (2020).
18. H. H. Xiao, G. Q. Ma, J. Y. Tan, S. Ru, Z. Q. Ai and C. X. Wang, *RSC Adv.*, **10**, 32609 (2020).
19. J. R. Jesus, J. G. S. Duque, C. T. Meneses, R. J. S. Lima and K. O. Moura, *Ceram. Int.*, **44**, 3585 (2018).
20. B. Lin, H. Li, H. An, W. B. Hao, J. J. Wei, Y. Z. Dai, C. S. Ma and G. D. Yang, *Appl. Catal. B*, **220**, 542 (2018).
21. F. Tian, H. P. Zhao, G. F. Li, Z. Dai, Y. L. Liu and R. Chen, *ChemSusChem.*, **9**, 1579 (2016).
22. F. Ji, J. Li, X. L. Cui, J. Liu, X. M. Bing and P. Song, *Appl. Clay. Sci.*, **162**, 182 (2018).
23. Y. J. Long, L. X. Li, L. T. Zhou, S. F. Zhang, L. L. Wang, Z. G. Zheng, S. L. Wu, Y. R. Hei and F. Z. Jiang, *Mater. Res. Bull.*, **126**, 110787 (2020).
24. Z. S. Li, S. Y. Yang, J. M. Zhou, D. H. Li, X. F. Zhou, C. Y. Ge and Y. P. Fang, *Chem. Eng. J.*, **241**, 344 (2014).
25. W. D. Hou, C. M. Deng, H. M. Xu, D. Y. Li, Z. W. Zou, H. Xia and D. S. Xia, *ChemistrySelect.*, **5**, 2767 (2020).
26. Y. G. Li, W. K. Shang, H. J. Li, M. R. Yang, S. S. Shi, J. Li, C. Y. Huang and A. N. Zhou, *ChemistrySelect.*, **6**, 4319 (2021).
27. D. Y. Jiang, D. Xu, J. Zheng, Y. Yang, C. Liu, Y. S. Wang, G. B. Che, X. Lin and L. M. Chang, *J. Chem. Phys.*, **29**, 600 (2016).
28. H. J. Fang, Y. S. Pan, H. X. Yan, L. F. Xu and C. L. Pan, *Mater. Sci. Semicond. Process.*, **127**, 105722 (2021).
29. X. Q. Hao, Q. J. Guo, M. Li, Z. L. Jin and Y. Wang, *Catal. Sci. Technol.*, **10**, 5267 (2020).
30. H. J. Zhao, Z. Yu, R. J. Wu, M. Yi, G. H. Zhang, Y. Zhou, Z. B. Han, X. Li and F. Ma, *J. Chin. Chem. Soc.*, **69**, 925 (2022).
31. M. Khajeh, A. R. Oveisi, A. Barkhordar, M. Rakhshanipour and H. Sargazi-Avval, *J. Nanostructure. Chem.*, **12**, 105 (2022).
32. J. F. Chen, J. B. Zhong, S. T. Huang, J. Z. Li and R. Duan, *Inorg. Nano-Met. Chem.*, **52**, 563 (2021).
33. X. B. Li, J. Xiong, Y. Xu, Z. J. Feng and J. T. Huang, *Chin. J. Catal.*, **40**, 424 (2019).
34. M. S. Zhu, Z. C. Sun, M. Fujitsuka and T. Majima, *Angew. Chem. Int. Ed. Engl.*, **57**, 2160 (2018).
35. S. J. Li, J. L. Chen, S. W. Hu, H. L. Wang, W. Jiang and X. B. Chen, *Chem. Eng. J.*, **402**, 126165 (2020).
36. R. Pandiyan, Z. Oulad Elhmaidi, Z. Sekkat, M. Abd-lefdil and M. A. El Khakani, *Appl. Surf. Sci.*, **396**, 1562 (2017).
37. Y. L. Gao, *Mater. Sci. Eng. R.*, **68**, 39 (2010).
38. Q. L. Xu, L. Y. Zhang, J. G. Yu, S. Wageh, A. A. Al-Ghamdi and M. Jaroniec, *Mater. Today*, **21**, 1042 (2018).
39. J. J. Liu, B. Cheng and J. G. Yu, *Phys. Chem. Chem. Phys.*, **18**, 31175 (2016).